

Selective Hydroxylation of In_2O_3 as A Route to Site-Selective Atomic Layer Deposition

Nannan Shan,¹ Jessica Catharine Jones,¹ Chunxin Luo,² Adam S. Hock,^{1,2} Alex B. F. Martinson,^{1,*} Lei Cheng^{1,*}

¹Materials Science Division, Argonne National Laboratory, Lemont, IL, 60439, USA

²Department of Chemistry, Illinois Institute of Technology, Chicago, Illinois 60616, USA

*Alex B. F. Martinson: martinson@anl.gov

*Lei Cheng: leicheng@anl.gov

Abstract

Several atomic layer deposition (ALD) processes are now known that leverage the distinct surface chemistry of two disparate substrates (e.g. metal vs. oxide) to realize markedly different ALD nucleation rates in an approach referred to as area-selective ALD (AS-ALD). In contrast, few ALD processes have been identified that allow selective reaction at distinct surface sites of a single material surface, in a process that might be called site-selective ALD (SS-ALD). We describe one potential strategy to discriminate among several distinct surface sites on bixbyite In_2O_3 to achieve site selectivity. Using density functional theory (DFT) we predict the discriminant hydration and hydroxylation of In_2O_3 terrace and step-edge sites that depends strongly on the substrate temperature at low water coverage. Infrared measurement of surface hydroxyls on In_2O_3 nanoparticles support the predicted temperature dependence. The *in situ* examination of MgO ALD nucleation also shows results consistent with the predicted temperature dependence of In_2O_3 hydroxylation. Together, these findings suggest that a selective hydroxylation approach may be a viable route to SS-ALD on In_2O_3 .

1. Introduction

Area-selective atomic layer deposition (AS-ALD) processes have been developed, and recently reviewed, that achieve strikingly different ALD nucleation rates on disparate substrates (e.g. metals vs. oxides).¹⁻⁴ In contrast, very few ALD processes have been identified that hint at even more subtle synthetic control in which deposition reactions are directed exclusively to distinct surface sites of a single material surface, a process that may be referred to as site-selective ALD (SS-ALD). We propose a SS-ALD strategy that leverages the unique activity (e.g. hydration/hydroxylation) of defect sites which differ from more ideal terrace surface sites. This defect-selective approach may be useful for targeting and remediating electronic defects that may otherwise get buried at optoelectronic device interfaces.⁵⁻⁶ This precise surface synthesis approach differs from the common ALD practice of applying synthesis and processing conditions optimized for thin film growth to interface synthesis. A vast literature of ALD synthesis has been developed to produce thin films with compositions that span the periodic table.⁷⁻⁸ However, applying the optimal synthesis conditions for growing a thin film to initiating an interface is a lost opportunity, as the presenting substrate is likely to present surface structure and chemistry that is quite distinct from the growing ALD film front. In short, a general approach to selective control of growth on specific surface sites inherited from unique surface site reactivity remains an unmet challenge for ALD science.

A representative oxide ALD cycle consists of two half-reactions in which the metal and oxygens are added sequentially. In the first half-cycle, metal deposition is often completed through the reaction of a metal-organic precursors with surface hydroxyl groups. A temperature-dependent surface hydroxyl density has previously been invoked to rationalize the temperature-dependent growth rate of several oxide ALD processes.⁹ However, the precise facet- and defect-specific hydration of metal oxide substrates, and its implications for ALD growth, remains underexplored. In one notable exception, Terranova and Bowler computationally studied the incomplete hydration of a defective TiO₂ anatase (101) facet to rationalize the incomplete coverage of ALD Al₂O₃ observed experimentally.¹⁰ They used DFT to predict that under some common ALD processing conditions the hydration of a flat terrace site is unfavorable even while hydration of step-edges, O vacancies, and Ti interstitials remains favorable. However, the authors ultimately propose conditions under which they hope to achieve unselective, uniform deposition to provide more

complete coating coverage. In subsequent work by Jin et al., these computational predictions were used to inform experiments that indirectly demonstrate site-selective ALD, whereby reaction of with electronic surface defects led to more uniform charge transfer rates from quantum dot sensitizers into anatase TiO_2 .¹¹

Here we select In_2O_3 as a technologically relevant oxide for investigation, although we expect that the selective hydration strategy for SS-ALD may be broadly applicable to other metal oxide surfaces. In_2O_3 thin films continue to attract attention for myriad applications where both optical transparency and electrical conductivity are critical to device performance.¹²⁻¹³ We use DFT to predict the discriminant hydration and hydroxylation of In_2O_3 (111) terrace and (211) step-edge sites to occur over a range of ~ 900 K, which includes temperatures most relevant to ALD (< 350 °C). *In situ* infrared investigation of In_2O_3 nanoparticles corroborate a broad temperature range of dehydroxylation of surface defects. Furthermore, temperature-dependent ALD nucleation studies provide evidence that selective surface hydroxylation influences surface synthesis on In_2O_3 .

2. Methods

2.1 Computational details

Periodic and spin-polarized DFT calculations were performed using the VASP code¹⁴⁻¹⁵ with the exchange–correlation potential described with the Perdew-Burke-Ernzerhof (PBE) functional.¹⁶ The 4d, 5s and 5p states of In and 2s and 2p states of O are explicitly treated as valence states within the projector augmented wave (PAW) method.¹⁷ In the present work, the Hubbard-U corrections¹⁸ were not included for In 4d electrons, given the fact that the U corrections exhibited minimum effect on the valence band close to the Fermi level, which is dominated by O 2p and In 5s states.¹⁹⁻²⁰ For the surface model, the Kohn-Sham orbitals were expanded based on a plane-wave basis set with a cutoff energy of 400 eV. The reciprocal Brillouin zone integrations were performed using a $2 \times 2 \times 1$ k-point mesh within Monkhorst–Pack grid.²¹ For the calculation of density of states, a $7 \times 7 \times 1$ k-point grid was used. The Gaussian smearing was implemented with a width of 0.02 eV. The electronic convergence threshold of 10^{-6} eV was used, whereas the force convergence criterion for ionic relaxation was 0.02 eV/Å. Dipole corrections were included in all calculations since only one side of the surface was allowed to react with the adsorbates.

To evaluate the hydration conditions of various In_2O_3 surfaces, the adsorption of water on terrace sites of (111) and step-edges sites of (211) were investigated. The adsorption energy of water, ΔE_{H_2O} , was defined as,

$$\Delta E_{H_2O} = E_{H_2O^*} - E_* - E_{H_2O_{gas}}, \quad (1)$$

where $E_{H_2O^*}$, E_* , and $E_{H_2O_{gas}}$ are the energies of water adsorbed on the surface, the original surface and the water molecule in the gas phase. The adsorption free energy of water, ΔG_{H_2O} , was estimated using Equation (2) as reported in previous works²²⁻²⁴ and the Atomic Simulation Environment (ASE) tools,²⁵

$$\Delta G_{H_2O} = \Delta E_{H_2O} + \Delta E_{ZPE} + \int_0^T \Delta C_p dT - T \times \Delta S, \quad (2)$$

where ΔE_{ZPE} is the zero-point energy change computed from vibrational frequencies based on the harmonic oscillator model, $\int_0^T \Delta C_p dT$ the heat capacity change at a constant pressure, T the temperature and ΔS the entropy changes of the adsorption. Specifically, the translational, rotational and vibrational entropies of gas phase species were calculated based on statistical mechanics²³, while only vibrational entropy was included and the translational and rotational entropies were approximated to be zero for surface adsorbates. In this work, we aim to establish the boundary conditions for hydration/dehydration. As the adsorptions are strongest (most negative ΔE_{H_2O}) at low coverages, only low-coverage adsorptions were studied. On $\text{In}_2\text{O}_3(111)$ and $\text{In}_2\text{O}_3(211)$ surface supercells, only one adsorbed water molecule was included, resulting in a 1/16 monolayer (ML) coverage.

The bixbyite $\text{In}_2\text{O}_3(111)$ and $\text{In}_2\text{O}_3(211)$ surfaces were adopted to represent the lowest energy (111) facet/terrace and a heavily miscut (111) surface with a high density of step-edges, respectively. Although other low index surfaces might have step-edges as well, we chose (211) as a representative to demonstrate the site-selective approach. Similar models have been applied in previous works.^{13, 26} The (1×1) $\text{In}_2\text{O}_3(111)$ surface slab consists of four O_{12} – In_{16} – O_{12} trilayers

stacked in the z-direction as shown Figure 1(a). In the surface O_{12} – In_{16} – O_{12} sandwich trilayer, four of the 16 In atoms are 6-fold coordinated In (i.e. In_{6c} in pink) and twelve are 5-fold coordinated In (i.e. In_{5c} in purple), Figure 1(b). The oxygen atoms in the upper most layer are 3-fold coordinated (i.e. O_{3c} in blue), while twelve oxygen atoms in the lower O layer are 4-fold coordinated (i.e. O_{4c} in dark blue).

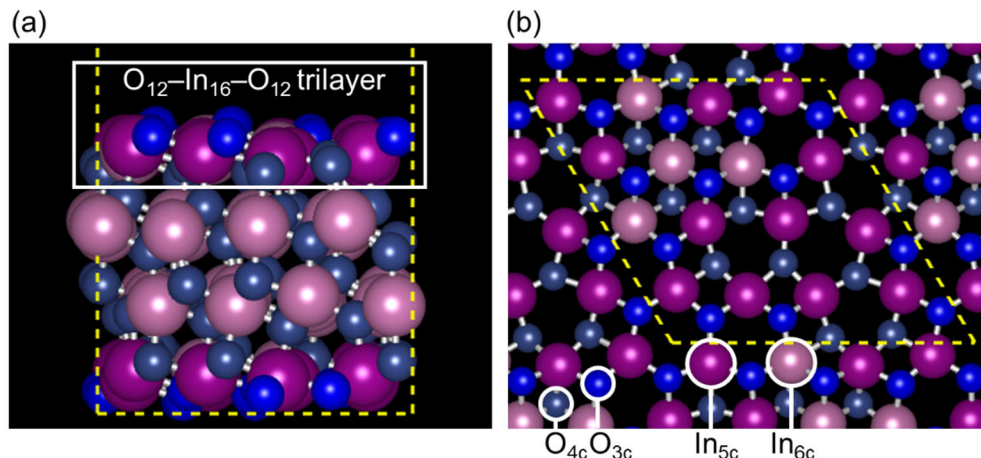


Figure 1. (a) Side view of the slab model used for $In_2O_3(111)$ surface, including four O_{12} – In_{16} – O_{12} trilayers. The top trilayer is marked with a white rectangle. (b) Top view of (111) surface with only the top O_{12} – In_{16} – O_{12} trilayer shown for clarity. The In_{5c} , In_{6c} , O_{3c} and O_{4c} atoms are in purple, pink, blue and dark blue, respectively. The yellow dashed lines are the periodic boundaries of the surface slab model.

During optimization, the bottom two trilayers are kept fixed at the optimized bulk lattice parameter of 10.31 Å (the experimental lattice parameter of cubic bixbyite In_2O_3 bulk is 10.12 Å²⁷), while the top two trilayers along with the adsorbates are allowed to relax. A vacuum layer of 20 Å in the z-direction was utilized to avoid the interaction between two repeated slabs. Convergence tests showed an adsorption energy difference of < 0.01 eV for molecular water using a slab model of 5 trilayers.

A (211) slab model with four trilayers and a 20 Å vacuum in z-direction was used to model a (111) surface with a high density of step-edge sites, as shown in Figure 2(a). A top view of the surface

is also presented in Figure 2(b) to show the surface sites more clearly. At the step-edge, heavily under-coordinated In_{4c} (dark rose) and O_{2c} (light blue) are present.

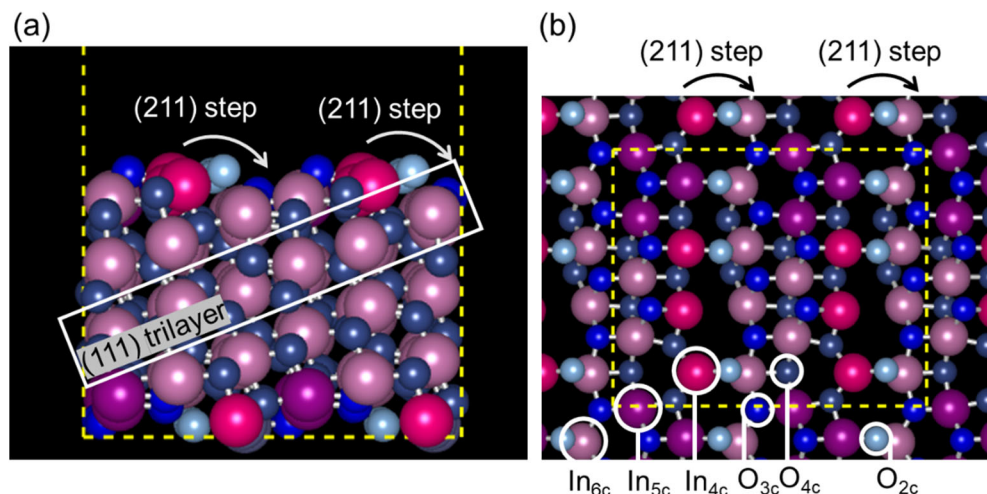


Figure 2. (a) Side view of the $\text{In}_2\text{O}_3(211)$ surface slab model with (111) trilayer labeled in a white rectangle. The (211) surface serves as a model of a heavily miscut (111) slab. The two step-edges are labeled with arrows for clarity. (b) Top view of the (211) surface with only the top trilayer atoms shown for clarity. The In_{4c} , In_{5c} , In_{6c} , O_{2c} , O_{3c} and O_{4c} atoms are in dark rose, purple, pink, light blue, blue and dark blue, respectively. The yellow dashed lines are the periodic boundaries of the slab model.

We note that different terminations can be obtained in constructing the (211) surface depending on the cut locations from bulk. These different cuts result in different numbers of 2-fold coordinated O (i.e. O_{2c}) on the step-edge sites. We obtained four distinct (211) models with different surface terminations and chose to investigate the one with the lowest surface energy, $0.086 \text{ eV}/\text{\AA}^2$, as calculated using the formulation reported by Hameeuw et al.²⁸ The other three models, with surface energies of $0.087 \text{ eV}/\text{\AA}^2$, $0.090 \text{ eV}/\text{\AA}^2$ and $0.091 \text{ eV}/\text{\AA}^2$, are shown in Figure S1.

2.2 Experimental details

Commercial boron-doped Si(100) substrates were scored from a larger wafer and degreased by sonication in acetone and then isopropanol and then blown dry with N_2 . A commercial ALD system

(Cambridge Nanotech, Inc., Savannah 200) was used to deposit In_2O_3 by alternating pulses of trimethylindium and O_3 from a corona arc discharge generator (DelOzone) which produces ~ 5 wt% percent O_3 in O_2 from high-purity O_2 delivered at 0.4 l/min during dosing. Final In_2O_3 film thicknesses were determined via *ex situ* spectroscopic ellipsometry (alpha-SE, J. A. Woollam). The crystallinity of the as-deposited films was determined by X-ray diffraction (XRD) on a Bruker Advance D8Powder X-ray Diffractometer with Ni-filtered $\text{Cu K}\alpha$ radiation operating at 40 kV and 40 mA. The scan range was between 15° and 60° with 0.0047° steps at a collection speed of 1 s/step.

In_2O_3 -coated Si samples were then introduced into a commercial ALD reactor (Cambridge Nanotech Inc., Fiji) where the walls were set to 300°C and the chuck was set to 250°C . This corresponded to a surface temperature of 252°C (525 K) for deposition of MgO via alternate dosing of bis(ethylcyclopentadienyl)magnesium ($\text{Mg}(\text{EtCp})_2$) and water vapor under 200 sccm of Ar gas. Ar gas (99.999%) is used as the carrier gas after passing through an Entegris GateKeeper I Series filter to remove water or carbon dioxide contamination down to parts per billion levels. A standard ALD recipe of t1-t2-t3-t4 was used where t1 is the exposure time of $\text{Mg}(\text{C}_5\text{H}_4\text{C}_2\text{H}_5)_2$, t2 is the purge time, t3 is the water pulse and t4 is the purge. The recipe used here (6-60-2-300 s), was selected to provide $\sim 2\times$ larger doses than those required for saturating growth of MgO ALD on MgO at 252°C (525 K) to further promote the saturation of interface reactions. The $\text{Mg}(\text{EtCp})_2$ cylinder was held at 110°C while no other precursors were intentionally heated. The MgO nucleation rate was deduced from *in situ* spectroscopic ellipsometry (M2000, J. A. Woollam) collected with a ~ 5 sec sampling rate.

The relative hydration of commercially available crystalline In_2O_3 nanopowder (<100 nm particle size, Sigma Aldrich) was evaluated with variable-temperature infrared spectroscopy (Nexus 470) equipped with a praying mantis cell (Harrick) under air or 99.9999% N_2 . The temperature was ramped from 25 to 500°C (298 to 773 K) at 5°C per minute with spectra acquired every 5°C . Differential infrared spectra were first baseline shifted by their absorbance at 3800 cm^{-1} and subsequently subtracted from the final spectra at 500°C . The peak from 3600 cm^{-1} to 2400 cm^{-1} (assigned to In-OH at various sites) was integrated to estimate OH coverage.

3. Results and discussion

3.1 Selective hydration of In₂O₃ terrace and step-edge sites

The adsorption of H₂O on different In_{5c} sites on the In₂O₃(111) surface was calculated using the DFT method. Water can adsorb in a molecular form (molecular adsorption, hydration), or dissociate readily into OH and H on the surface (dissociative adsorption, hydroxylation), as commonly observed in previous works.²⁹⁻³² The kinetic barrier to dissociative adsorption of H₂O (i.e. reaction with the In₂O₃ surfaces) was not evaluated here.

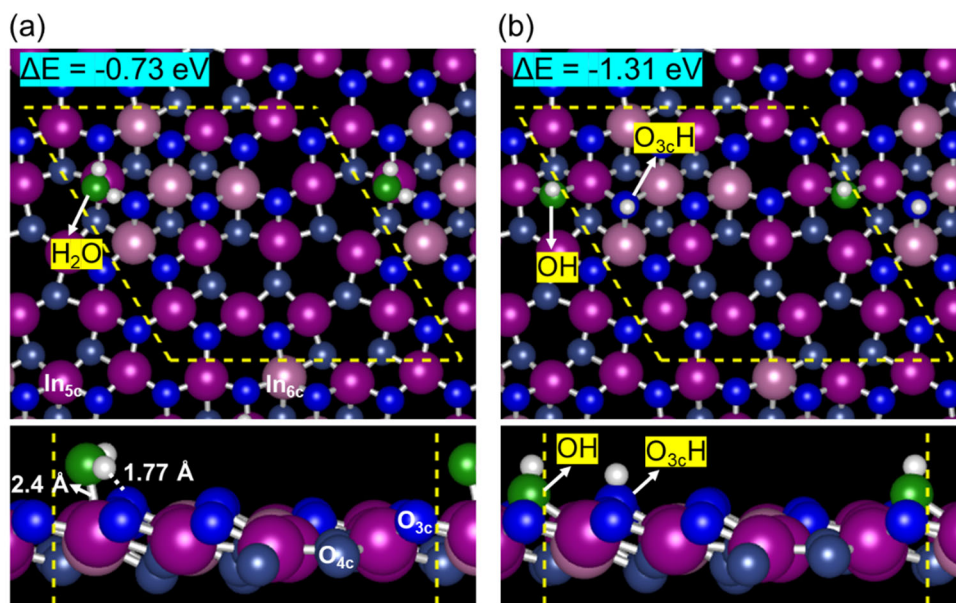


Figure 3. The most stable geometry of (a) molecular and (b) dissociative H₂O adsorption on In₂O₃(111). In_{5c}, In_{6c}, O_{3c} and O_{4c} atoms are shown in purple, pink, blue and dark blue, respectively. The O and H atoms of the H₂O molecule are green and white, respectively.

In the most stable geometry for molecular H₂O adsorption, Figure 3(a), H₂O binds to a surface In_{5c} atom with 2.4 Å between O (in H₂O) and In_{5c}. One H is further stabilized by a surface O_{3c}, forming an H-bond with a length of 1.77 Å. This geometry is in agreement with one previous reported by Diebold et al.³¹ The ΔE_{H_2O} for this adsorption geometry is -0.73 eV, also in close agreement with Diebold's work. In the most favorable dissociative adsorption geometry, Figure 3b, the dissociated H is adsorbed to a surface O_{3c}, while the remaining OH bridges two In_{5c} atoms. The ΔE_{H_2O} of the dissociative H₂O adsorption, -1.31 eV, is more favorable than the molecular adsorption on the

terrace sites of $\text{In}_2\text{O}_3(111)$. This predicted dissociative single H_2O configuration agrees with Diebold's report but with a slightly stronger adsorption energy, i.e. -1.31 eV vs. -1.28 eV.

Molecular and dissociative H_2O adsorption on the $\text{In}_2\text{O}_3(211)$ surface, which serves as a proxy for step-edge sites that will be present on even the most perfectly prepared $\text{In}_2\text{O}_3(111)$ surface, was also investigated. H_2O prefers to adsorb on the low-coordination In_{4c} sites as shown in Figure 4(a).

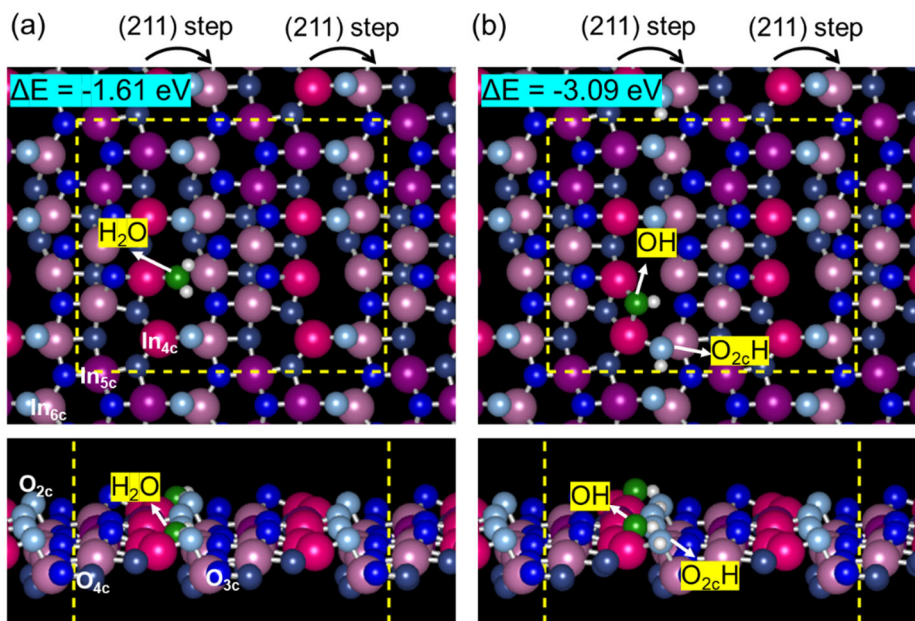


Figure 4. The most favorable configurations of (a) molecular and (b) dissociative H_2O adsorption on $\text{In}_2\text{O}_3(211)$ surface. Atom color coding as in previous figures.

The molecular H_2O adsorbs parallel to the planes of the steps with two H atoms pointing to the direction of the lower terrace. The $\Delta E_{\text{H}_2\text{O}}$ was calculated as -1.61 eV, indicating a much stronger adsorption than either the molecular (-0.73 eV) or dissociative (-1.31 eV) adsorption of H_2O to $\text{In}_2\text{O}_3(111)$ terraces. However, an even more stable dissociative configuration ($\Delta E_{\text{H}_2\text{O}} = -3.09$) was identified at step-edge sites via OH bridging over two adjacent In_{4c} sites and H on the proximal O_{2c} atom, Figure 4b. The adsorption of H_2O on the second stable (211) surface was evaluated as well. The geometries can be found in Figure S2(a-b). The calculated $\Delta E_{\text{H}_2\text{O}}$ on this (211) surface are less negative than those shown in Figure 4.

The hydration and hydroxylation of In_2O_3 surfaces will depend on the intrinsic interactions between water and surface sites as well as substrate temperature and H_2O partial pressure. The effect of temperature and pressure can be modeled with adsorption free energy ($\Delta G_{\text{H}_2\text{O}}$, Equation 2) calculations, with the caveat that adsorption energies are calculated at the lowest coverage (as low as 1/16 ML) allowed by our models. Furthermore, we do not consider the kinetics of adsorption or desorption in this study such that $\Delta G_{\text{H}_2\text{O}}$ captures only the thermodynamic of surface hydration/hydroxylation. This approximation was made based on a previous study showing low H_2O adsorption and desorption barriers on the In_2O_3 surface³³ and other literature studies showing generally facile H_2O adsorption and desorption kinetics on oxide surfaces.³⁴⁻³⁶ A partial pressure dependence study of $\Delta G_{\text{H}_2\text{O}}$, Figure S3, illustrates that larger water doses create more favorable conditions for hydration/hydroxylation at a given temperature, as expected. In the temperature dependence study of $\Delta G_{\text{H}_2\text{O}}$, a computational water partial pressure of 0.01 torr is utilized to approximate the partial pressure of water applied during each complete ALD cycle. The temperature-dependent free energies of water adsorption on terrace sites (i.e. $\text{In}_2\text{O}_3(111)$) and step-edge sites (i.e. $\text{In}_2\text{O}_3(211)$), Figure 5, reveals the wide range of temperatures at which H_2O adsorption becomes thermodynamically unfavorable for each surface site.

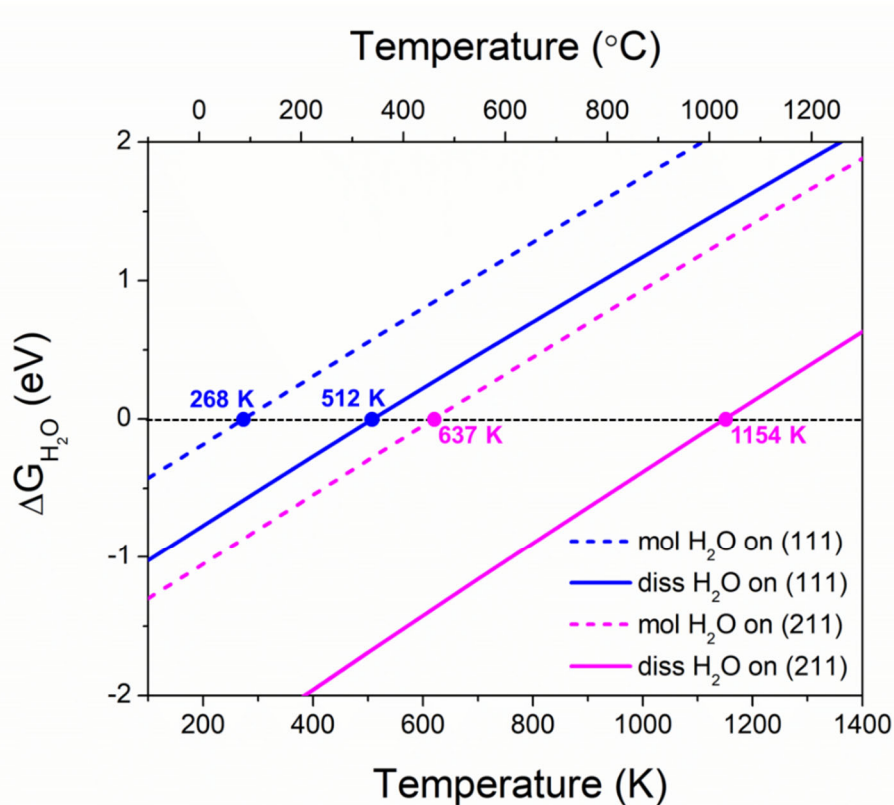


Figure 5. Adsorption free energies, ΔG_{H_2O} , of molecular (dashed) and dissociative (solid) H_2O on $In_2O_3(111)$ and $In_2O_3(211)$, blue and magenta, respectively. The horizontal dotted black line represents the threshold for favorable water (de)sorption from the surfaces.

The temperature at which hydroxylation of $In_2O_3(111)$ terrace sites becomes unfavorable is 512 K. However, hydrated $In_2O_3(211)$ step-edge remain favorable until 637 K and hydroxylation until 1154 K. This analysis reveals a temperature window (> 120 K) where hydration and hydroxylation of terrace sites is disfavored while both step-edge hydration and hydroxylation are favored. The computational study further reveals a wide selective hydroxylation window larger than 600 K where neither hydration nor hydroxylation is favored on terrace sites but hydroxylation remains favored on step-edges.

3.2 Infrared Investigation of the Dehydration of In_2O_3

In_2O_3 surface hydration was experimentally probed using variable-temperature infrared spectroscopy, monitoring and integrating the relative intensity of the O-H stretching region (3600 cm^{-1} to 2400 cm^{-1}). Two distinct regions of OH loss are observed as the sample is heated, Figure

6. In order to provide the best baseline, the experimental spectra are referenced to (subtracted from) the highest temperature spectra acquired at ~ 773 K.

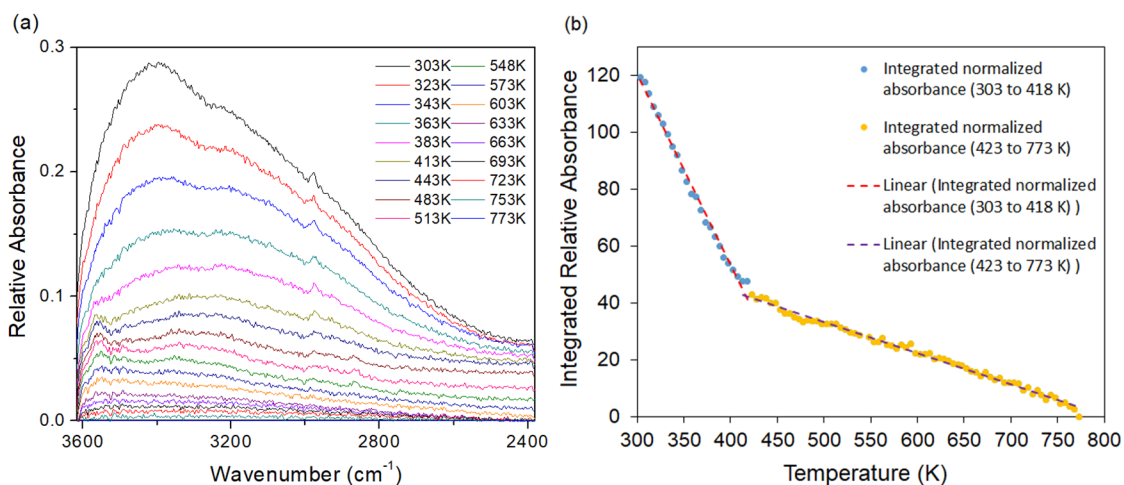


Figure 6. (a) Temperature-dependent infrared spectrum of nanoparticle In_2O_3 . The 773 K spectrum is subtracted from all raw data to produce relative absorbance spectra with optimal baseline. (b) Integrated relative OH absorbance versus temperature. The red and purple dash lines are linear fits to blue and yellow data, respectively.

The most rapid rate of OH loss is observed between 300 and 450 K, the same temperature range over which (111) terrace site hydroxylation is predicted to become unfavorable or minimally favorable. The loss of a much smaller population of surface hydroxide occurs at temperatures greater than 450 K. This behavior is consistent with DFT-predicted dehydration of the most stable step-sites characteristic of $\text{In}_2\text{O}_3(211)$. Note that the integrated relative absorbance of zero at 775K is not inconsistent with our prediction for favorable hydroxylation of the (211) terrace up to 1154K, since we define the relative integrated hydroxylation intensity to be that relative to the final 775K spectra we measure. However, a small OH population may remain at higher temperatures. We emphasize that the commercial nanoparticle In_2O_3 powder utilized for these experiments presents only a very crude approximation of the ideal $\text{In}_2\text{O}_3(111)$ and $\text{In}_2\text{O}_3(211)$ surfaces modeled computationally. Low Miller index surfaces follow the stability order $(111) > (110) > (100)$ ²⁶ that favors (111) faceted nanoparticles. On the other hand, several other facets, edges, and defects are also likely to be present. Still, the broad trends in In_2O_3 dehydroxylation as deduced from infrared spectroscopy support the computational prediction that In_2O_3 hydration and hydroxylation become

less favorable at higher temperature and is site-specific such that dehydration/dehydroxylation is stretched over more than a 400 K temperature window.

3.3 Deposition of MgO on In₂O₃

The computational predictions of In₂O₃ surface hydroxylation might further be corroborated through surface reaction with metalorganic precursors in hydroxyl-mediated ALD-type reactions. Mg(EtCp)₂, which is known to grow MgO upon alternate dosing with H₂O in an ALD process that occurs, at least in part, through a surface hydroxyl-mediated mechanism.⁹ Highly-oriented In₂O₃ bixbyite films were grown by ALD of trimethylindium and ozone at 250 °C to 30 nm thickness on Si substrates, as shown by X-ray diffraction (Figure S5) and spectroscopic ellipsometry. This relatively high temperature In₂O₃ process was previously reported to produce highly oriented films with (111) planes film surface.³⁷ The temperature dependence of In₂O₃ substrate hydration was indirectly investigated by nucleation of Mg(CpEt)₂ and water vapor at two different temperatures, 430 K (157 °C) and 525 K (252 °C). Previous infrared studies provide evidence for an MgO ALD mechanism in surface hydroxyl groups react with Mg(CpEt)₂ to release one or more HCpEt as a reaction product.⁹ Therefore we hypothesize that nucleation/growth of the MgO ALD process will be hindered in the absence of In₂O₃ surface hydroxyls. *In situ* ellipsometric analysis of MgO ALD on (111)-oriented In₂O₃ reveals nucleation/growth rates that are significantly lower than those for a SiO₂-terminated Si wafer control that is expected to exhibit significantly more hydroxylation at these temperatures³⁸⁻³⁹, Figure 7. Figure 7(a) shows the calculated MgO thickness, where 7(b) shows the MgO growth of each cycle as calculated by the change in thickness from (a). Steady-state growth (~0.12 nm/cycle) on itself (MgO) is achieved after 10 – 15 cycles on Si. In contrast, significantly lower growth rates characteristic of poor nucleation are observed on In₂O₃ in early cycles, and steady state growth is still not achieved after 20 cycles on In₂O₃. Based on our calculations and ALD experimental observations, it is also unlikely that other mechanisms bypassing the hydroxyl pathway contribute significantly to the growth at these temperatures.

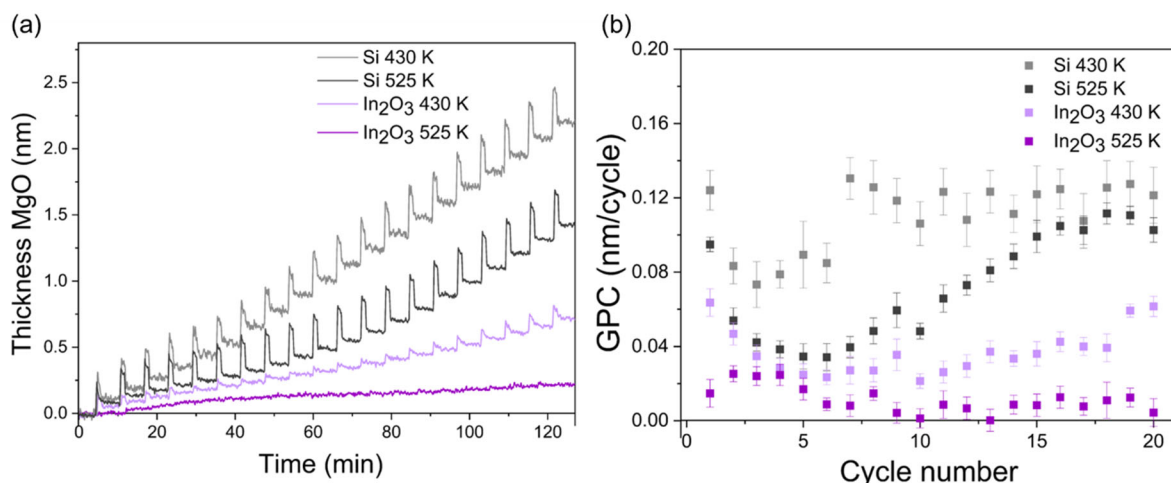


Figure 7. (a) The thickness of MgO deposited on In₂O₃ at 430 K and 525 K is shown in the light and dark purple traces respectively, and MgO deposited on bare Si at 430 K and 525 K is shown in the light and dark grey traces respectively. 5 points of adjacent-averaging smoothing is applied to all traces in (a), and the average growth per cycle and standard deviation of the MgO thickness, plot (b), were calculated from plot (a).

Furthermore, the MgO ALD nucleation rates on In₂O₃ are observed to be strongly temperature dependent in the range of 430 to 525 K, in agreement with our DFT predictions and FTIR measurements. Growth at 525 K corresponds to a region of unfavorable hydration for In₂O₃(111) terrace sites as predicted by DFT (Figure 5) and as shown by infrared measurement of In₂O₃ nanoparticles (Figure 6). The very slow, but non-zero, nucleation suggests that a minority of “defective” surface sites (e.g. In₂O₃(211) step-edge sites) may remain to allow some foothold for MgO nucleation. This nucleation study further suggests that any thermodynamically favorable unselective reactions that bypass the protonation and ligand shedding mechanism are not kinetically competitive.

3.4 Modified electronic density of states (DOS) of step-edge sites

One potential application of site-selective ALD (SS-ALD) may be to passivate surface atomic arrangements which act as electronic defects on semiconducting oxides. We examined the DOS distribution of In₂O₃ surface sites to identify intra-gap states which may act as electronic traps in optoelectronic devices. We hypothesize that wide band gap oxides including MgO, Ga₂O₃, and Al₂O₃ proximally bonded to In₂O₃ defect surface sites might modify the energy level of some

electronic defects on the semiconductor surface to remove them from the bandgap. Three popular precursors, including trimethylaluminium, $\text{Al}(\text{CH}_3)_3$, trimethylgallium, $\text{Ga}(\text{CH}_3)_3$, and bis(methylcyclopentadienyl)magnesium, $\text{Mg}(\text{MeCp})_2$, were selected for reaction at (211) step-edge sites in our computational study. As detailed above, hydroxyls are predicted to exclusively terminate the step-edges (but not terraces) at temperatures from 512 to 1154 K. If the OH groups react with the ALD precursors via the widely known protonation and ligand shedding mechanism, and are further reacted with water to remove any remaining ligands, we posit that $\text{OAl}(\text{OH})_2$, $\text{OGa}(\text{OH})_2$ and OMgOH species could be formed on the step-edge sites of $\text{In}_2\text{O}_3(211)$. We calculate the density of states (DOS) of the second stable step-edge $\text{In}_2\text{O}_3(211)$ (see Figure S1a) surface before and after reaction with three metalorganic precursors and compare them with the terrace $\text{In}_2\text{O}_3(111)$ surface DOS in Figure 8.

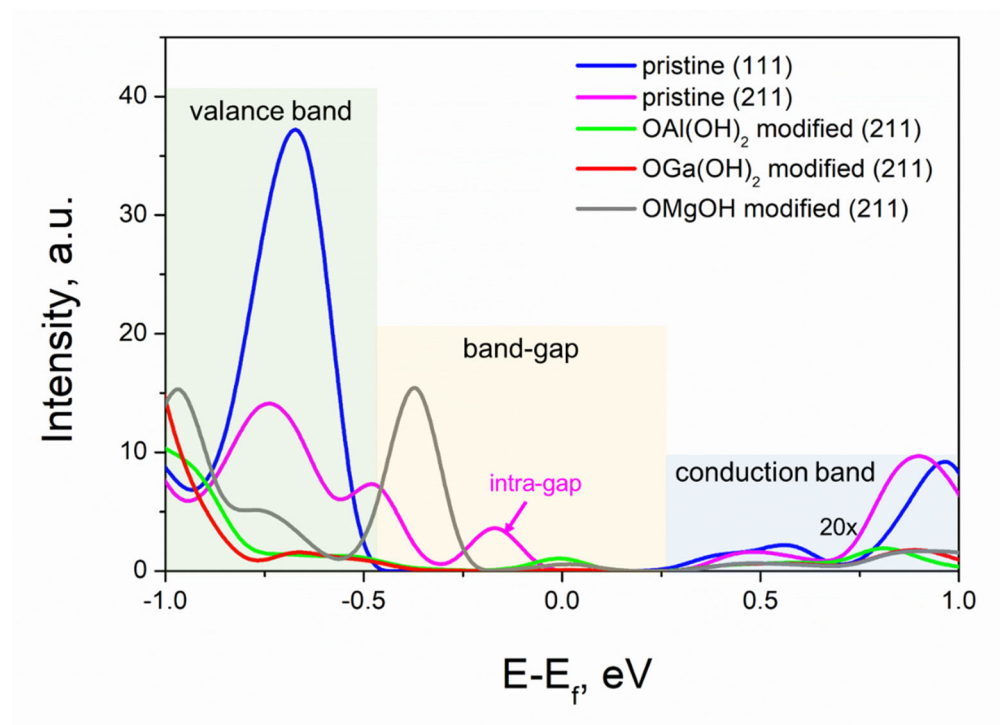


Figure 8. The density of states (DOSs) of pristine $\text{In}_2\text{O}_3(111)$ (in blue), pristine $\text{In}_2\text{O}_3(211)$ (in magenta), $\text{OAl}(\text{OH})_2$ on $\text{In}_2\text{O}_3(211)$ (in green), $\text{OGa}(\text{OH})_2$ on $\text{In}_2\text{O}_3(211)$ (in red) and OMgOH on $\text{In}_2\text{O}_3(211)$ (in grey). The conduction band intensity was amplified by 20 times for clarity.

The bandgap is 0.87 eV from DOS of In_2O_3 bulk based on the PBE functional calculations (Figure S6). It is consistent with the reported value using a similar method,¹⁹ although the experimental

bandgap is measured as 2.9 eV.⁴⁰ It is well-known that the bandgap from PBE functional is severely underestimated,⁴¹ however we investigate here only the changing trend in intra-gap state density, not the absolute energy levels. In addition, previous work have indicated PBE functional is able to capture the similar trend as HSE06 functional for the band gap estimations.⁴²⁻⁴³ The total and projected DOSs of In₂O₃(111) and In₂O₃(211) can be found in Figure S7. In all cases the valance band is dominated by O 2p states and the conducted band by In 5s states.

For the DOS comparison among pristine In₂O₃(111), pristine In₂O₃(211) and modified In₂O₃(211), the DOS intensity is extracted only from the atoms located in a small region of In₂O₃(211) step-edge structure, where In_{3c}, In_{4c}, In_{5c}, In_{6c}, O_{2c}, O_{3c} and O_{4c} atoms were all included (Figure 8). For pristine In₂O₃(211) (magenta lines), an intra-gap DOS is located below the Fermi level (ca. -0.50 ~ 0 eV), which is mainly derived from the under-coordinated O_{2c} atoms at the step-edge. However, after modification with OAl(OH)₂ and OGa(OH)₂ the intra-gap DOS is significantly reduced (green and red lines in Figure 8). In contrast, the addition of OMgOH is computationally predicted to increase the intra-gap DOS albeit at an energy level closer to the VB, -0.5 ~ -0.2eV. Therefore, the selective hydration/hydroxylation + ALD strategy may serve as viable route to targeted remediation of electronic defects for In₂O₃(111) surfaces.

However, the careful selection of metalorganic precursors is required and additional defects (i.e. oxygen vacancies, polycrystalline grain boundaries) need also be considered. Furthermore, multiple defect configurations may also require additional consideration. For example, the same analysis of the DOS states on the slightly more stable In₂O₃(211) surface (shown in Figure 2) reveals DOS states remain in the bandgap after modification by OAl(OH)₂, OGa(OH)₂ and OMgOH, Figure S8. As these two In₂O₃(211) configurations are so similar in energy (0.086 vs 0.087 eV/Å²), we speculate that the probability of obtaining these two configurations may be similar. As such, additional or alternative site-selective electronic defect remediation metals or strategies must be identified to further reduce electronic defect populations. We report the electronic structure modification of the second most stable (211) by ALD, as it directly addresses the hypothesis of this study, the potential of this surface approach for defect remediation.

4. Conclusions

In this work, we present a strategy for site-selective ALD (SS-ALD) on In_2O_3 . The predicted selectivity originates from the discriminant hydration/hydroxylation of step-edges over terrace sites at elevated temperatures. Using DFT calculations we predict the temperature and water partial pressure range over which such selectivity might be achieved. Infrared measurement of surface hydroxyls on In_2O_3 nanoparticles support the wide predicted temperature range for site-specific hydroxylation. *In situ* examination of MgO ALD also reveals a temperature dependence for nucleation rates consistent with a hydroxyl-mediated mechanism. Finally, we predict using DOS calculations that intra-gap states, which may act as electronic traps in optoelectronic devices, introduced by under-coordinated atoms at one low energy In_2O_3 (211) step-edge configuration could be selectively remediated by reaction with wide band-gap oxide precursors. However, similar modifications to another low energy In_2O_3 (211) step-edge configuration results in a shifted DOS that remains within the bandgap. We predict that the discriminant hydroxylation approach may be a general strategy for SS-ALD on oxide surfaces. However, even the computational remediation of myriad electronic defects on the surface of assorted oxides, each with several facets and low energy defect configuration, will require significantly more study and additional strategies.

Supporting Information

Structures of less stable (211) surfaces, H_2O adsorptions on the second stable (211) surfaces, full spectrum raw infrared data, X-Ray Diffraction of In_2O_3 deposited on Si(100), projected DOSs of In_2O_3 bulk, $\text{In}_2\text{O}_3(111)$ and $\text{In}_2\text{O}_3(211)$, and modified DOS of the most stable (211).

Acknowledgement

This work was primarily supported by the U.S. Department of Energy, Office of Science, Basic Energy Sciences, Materials Science and Engineering Division. N.S. and C.L. acknowledge computational supports from Bebop cluster of Laboratory Computing Resource Center (LCRC), Carbon cluster of Center for Nanoscale Materials (CNM) at Argonne National Laboratory supported by the Office of Science of the US Department of Energy under the contract No. DE-AC02-06CH11357, and National Energy Research Scientific Computing Center (NERSC) supported by U.S. Department of Energy Office of Science under Contract No. DE-AC02-05CH11231.

Reference

1. Mackus, A. J. M.; Merks, M. J. M.; Kessels, W. M. M. From the bottom-up: toward area-selective atomic layer deposition with high selectivity. *Chem. Mater.* **2019**, *31*, 2-12.
2. Parsons, G. N.; Clark, R. D. Area-selective deposition: fundamentals, applications, and future outlook. *Chem. Mater.* **2020**, *32*, 4920-4953.
3. Liu, T.-L.; Bent, S. F. Area-selective atomic layer deposition on chemically similar materials: achieving selectivity on oxide/oxide patterns. *Chem. Mater.* **2021**, *33*, 513-523.
4. Cao, K.; Cai, J.; Chen, R. Inherently selective atomic layer deposition and applications. *Chem. Mater.* **2020**, *32*, 2195-2207.
5. Flynn, C. J.; McCullough, S. M.; Oh, E.; Li, L.; Mercado, C. C.; Farnum, B. H.; Li, W.; Donley, C. L.; You, W.; Nozik, A. J., et al. Site-selective passivation of defects in NiO solar photocathodes by targeted atomic deposition. *ACS Appl. Mater. Interfaces* **2016**, *8*, 4754-4761.
6. Flynn, C. J.; McCullough, S. M.; Li, L.; Donley, C. L.; Kanai, Y.; Cahoon, J. F. Passivation of nickel vacancy defects in nickel oxide solar cells by targeted atomic deposition of boron. *J. Phys. Chem. C* **2016**, *120*, 16568-16576.
7. Miikkulainen, V.; Leskelä, M.; Ritala, M.; Puurunen, R. L. Crystallinity of inorganic films grown by atomic layer deposition: Overview and general trends. *J. Appl. Phys.* **2013**, *113*, 021301.
8. George, S. M. Atomic Layer Deposition: An Overview. *Chem. Rev.* **2010**, *110*, 111-131.
9. Burton, B. B.; Goldstein, D. N.; George, S. M. Atomic layer deposition of MgO using bis(ethylcyclopentadienyl)magnesium and H₂O. *J. Phys. Chem. C* **2009**, *113*, 1939-1946.
10. Terranova, U.; Bowler, D. R. Effect of hydration of the TiO₂ anatase (101) substrate on the atomic layer deposition of alumina films. *J. Mater. Chem.* **2011**, *21*, 4197-4203.
11. Jin, S.; Martinson, A. B.; Wiederrecht, G. P. Reduced heterogeneity of electron transfer into polycrystalline TiO₂ films: site specific kinetics revealed by single-particle spectroscopy. *J. Phys. Chem. C* **2012**, *116*, 3097-3104.
12. Kim, H.; Gilmore, C. M.; Piqué, A.; Horwitz, J. S.; Mattoussi, H.; Murata, H.; Kafafi, Z. H.; Chrisey, D. B. Electrical, optical, and structural properties of indium-tin-oxide thin films for organic light-emitting devices. *J. Appl. Phys.* **1999**, *86*, 6451-6461.
13. Agoston, P.; Albe, K. Thermodynamic stability, stoichiometry, and electronic structure of bcc-In₂O₃ surfaces. *Phys. Rev. B* **2011**, *84*, 045311.
14. Kresse, G.; Furthmüller, J. Efficiency of ab-initio total energy calculations for metals and semiconductors using a plane-wave basis set. *Comput. Mater. Sci.* **1996**, *6*, 15-50.
15. Kresse, G.; Hafner, J. Ab initio molecular dynamics for open-shell transition metals. *Phys. Rev. B* **1993**, *48*, 13115-13118.
16. Perdew, J. P.; Burke, K.; Ernzerhof, M. Generalized gradient approximation made simple. *Phys. Rev. Lett.* **1996**, *77*, 3865-3868.
17. Blöchl, P. E. Projector augmented-wave method. *Phys. Rev. B* **1994**, *50*, 17953-17979.
18. Dudarev, S. L.; Botton, G. A.; Savrasov, S. Y.; Humphreys, C. J.; Sutton, A. P. Electron-energy-loss spectra and the structural stability of nickel oxide: An LSDA+U study. *Phys. Rev. B* **1998**, *57*, 1505-1509.
19. Posada-Borbón, A.; Grönbeck, H. Hydrogen adsorption on In₂O₃(111) and In₂O₃(110). *Phys. Chem. Chem. Phys.* **2020**, *22*, 16193-16202.
20. Erhart, P.; Klein, A.; Egdell, R. G.; Albe, K. Band structure of indium oxide: Indirect versus direct band gap. *Phys. Rev. B* **2007**, *75*, 153205.
21. Monkhorst, H. J.; Pack, J. D. Special points for Brillouin-zone integrations. *Phys. Rev. B* **1976**, *13*, 5188-5192.
22. Shan, N.; Hanchett, M. K.; Liu, B. Mechanistic insights evaluating Ag, Pb, and Ni as electrocatalysts for furfural reduction from first-principles methods. *J. Phys. Chem. C* **2017**, *121*, 25768-25777.

23. Le, T. N.-M.; Liu, B. Huynh, L. K. SurfKin: an ab initio kinetic code for modeling surface reactions. *J. Comput. Chem.* **2014**, *35*, 1890-1899.
24. Weckman, T. Laasonen, K. First principles study of the atomic layer deposition of alumina by TMA-H₂O-process. *Phys. Chem. Chem. Phys.* **2015**, *17*, 17322-17334.
25. Hjorth Larsen, A.; Jørgen Mortensen, J.; Blomqvist, J.; Castelli, I. E.; Christensen, R.; Dułak, M.; Friis, J.; Groves, M. N.; Hammer, B.; Hargus, C., et al. The atomic simulation environment—a Python library for working with atoms. *J. Phys.: Condens. Matter* **2017**, *29*, 273002.
26. Walsh, A. Catlow, C. R. A. Structure, stability and work functions of the low index surfaces of pure indium oxide and Sn-doped indium oxide (ITO) from density functional theory. *J. Mater. Chem.* **2010**, *20*, 10438-10444.
27. Marezio, M. Refinement of the crystal structure of In₂O₃ at two wavelengths. *Acta Crystallogr.* **1966**, *20*, 723-728.
28. Hameeuw, K. J.; Cantele, G.; Ninno, D.; Trani, F. Iadonisi, G. The rutile TiO₂ (110) surface: Obtaining converged structural properties from first-principles calculations. *J. Chem. Phys.* **2006**, *124*, 024708.
29. Bikondoa, O.; Pang, C. L.; Ithnin, R.; Muryn, C. A.; Onishi, H. Thornton, G. Direct visualization of defect-mediated dissociation of water on TiO₂(110). *Nat. Mater.* **2006**, *5*, 189-192.
30. Kristoffersen, H. H.; Hansen, J. Ø.; Martinez, U.; Wei, Y. Y.; Matthiesen, J.; Streber, R.; Bechstein, R.; Lægsgaard, E.; Besenbacher, F.; Hammer, B., et al. Role of steps in the dissociative adsorption of water on rutile TiO₂(110). *Phys. Rev. Lett.* **2013**, *110*, 146101.
31. Wagner, M.; Lackner, P.; Seiler, S.; Brunsch, A.; Bliem, R.; Gerhold, S.; Wang, Z.; Osiecki, J.; Schulte, K.; Boatner, L. A., et al. Resolving the structure of a well-ordered hydroxyl overlayer on In₂O₃(111): nanomanipulation and theory. *ACS Nano* **2017**, *11*, 11531-11541.
32. Shin, H.-J.; Jung, J.; Motobayashi, K.; Yanagisawa, S.; Morikawa, Y.; Kim, Y. Kawai, M. State-selective dissociation of a single water molecule on an ultrathin MgO film. *Nat. Mater.* **2010**, *9*, 442-447.
33. Lin, S. Xie, D. Initial decomposition of methanol and water on In₂O₃(110): a periodic DFT study. *Chin. J. Chem.* **2012**, *30*, 2036-2040.
34. Tilocca, A. Selloni, A. Reaction pathway and free energy barrier for defect-induced water dissociation on the (101) surface of TiO₂-anatase. *J. Chem. Phys.* **2003**, *119*, 7445-7450.
35. Xu, H.; Zhang, R. Q.; Ng, A. M. C.; Djurišić, A. B.; Chan, H. T.; Chan, W. K. Tong, S. Y. Splitting water on metal oxide surfaces. *J. Phys. Chem. C* **2011**, *115*, 19710-19715.
36. Shavorskiy, A.; Eralp, T.; Ataman, E.; Isvoranu, C.; Schnadt, J.; Andersen, J. N. Held, G. Dissociation of water on oxygen-covered Rh{111}. *J. Chem. Phys.* **2009**, *131*, 214707.
37. Mane, A. U.; Allen, A. J.; Kanjolia, R. K. Elam, J. W. Indium oxide thin films by atomic layer deposition using trimethylindium and ozone. *J. Phys. Chem. C* **2016**, *120*, 9874-9883.
38. Sneh, O. George, S. M. Thermal stability of hydroxyl groups on a well-defined silica surface. *J. Phys. Chem.* **1995**, *99*, 4639-4647.
39. Tong, Q.; Lee, T.; Gösele, U.; Reiche, M.; Ramm, J. Beck, E. The role of surface chemistry in bonding of standard silicon wafers. *J. Electrochem. Soc.* **1997**, *144*, 384-389.
40. Walsh, A.; Da Silva, J. L. F.; Wei, S.-H.; Körber, C.; Klein, A.; Piper, L. F. J.; DeMasi, A.; Smith, K. E.; Panaccione, G.; Torelli, P., et al. Nature of the band gap of In₂O₃ revealed by first-principles calculations and X-Ray spectroscopy. *Phys. Rev. Lett.* **2008**, *100*, 167402.
41. Shishkin, M. Kresse, G. Self-consistent GW calculations for semiconductors and insulators. *Phys. Rev. B* **2007**, *75*, 235102.
42. Pilania, G.; Yadav, S. K.; Nikl, M.; Uberuaga, B. P. Stanek, C. R. Role of multiple charge states of Ce in the scintillation of ABO₃ perovskites. *Phys. Rev. Appl.* **2018**, *10*, 024026.
43. Lentz, L. C. Kolpak, A. M. Predicting HSE band gaps from PBE charge densities via neural network functionals. *J. Phys: Condens. Matter* **2020**, *32*, 155901.

